



Interaction-driven band flattening and correlated phases in twisted bilayer graphene

Youngjoon Choi^{1,2,3,7}, Hyunjin Kim^{1,2,3,7}, Cyprian Lewandowski^{2,3,4}, Yang Peng⁵, Alex Thomson^{2,3,4}, Robert Polski^{1,2}, Yiran Zhang^{1,2,3}, Kenji Watanabe⁶, Takashi Taniguchi⁶, Jason Alicea^{2,3,4} and Stevan Nadj-Perge^{1,2} ⊠

Flat electronic bands, characteristic of 'magic-angle' twisted bilayer graphene, host many correlated phenomena¹⁻⁹. Nevertheless, many properties of these bands and emerging symmetry-broken phases are still poorly understood. Here we use scanning tunnelling spectroscopy to examine the evolution of the twisted bilayer graphene bands and related gapped phases as the twist angle between the two graphene layers changes. We detect filling-dependent flattening of the bands that is appreciable even when the angle is well above the magic angle value and so the material is nominally in a weakly correlated regime. Upon approaching the magic angle, we further show that the most prominent correlated gaps begin to emerge when band flattening is maximized around certain integer fillings of electrons per moiré unit cell. Our observations are consistent with a model that suggests that a significant enhancement of the density of states caused by the band flattening triggers a cascade of symmetry-breaking transitions. Finally, we explore the temperature dependence of the cascade and identify gapped features that develop in a broad range of band fillings where superconductivity is expected. Our results highlight the role of interaction-driven band flattening in defining the electronic properties of twisted bilayer graphene.

Seminal theoretical considerations^{10,11} suggested that, when two graphene sheets are twisted at a particular magic angle of 1.1°, the Dirac velocity of the resulting twisted bilayer graphene (TBG) electronic bands vanishes and the entire bandwidth becomes extremely narrow. The resulting suppression of electron kinetic energy in turn promotes the development of strong electronic correlations. While various correlated phases are indeed identified in magic-angle TBG, experimental studies¹⁻⁹ reveal a finite Dirac velocity as well as bandwidths significantly larger than predicted. More sophisticated models that include critical TBG details such as atomic reconstruction, strain and interaction effects¹²⁻²³ can in part reconcile the observed band broadening, though the separation between theory and experiment persists. In particular, the effects of interactions are notoriously difficult to model at the magic angle and usually result in large discrepancies with experiments. Much better agreement is expected slightly away from the magic angle, where interactions and correlation effects are weaker and can potentially be captured using Hartree corrections¹⁹⁻²³ that predict significant filling-dependent flattening of the moiré bands. Moreover, recent theoretical considerations suggest that the band flattening in these regimes is linked to the formation of certain correlated phases²⁴. However, these TBG regimes, essential for understanding the relation between moiré bands and emerging correlated phases, have not been explored experimentally so far.

Figure 1a sketches our scanning tunnelling microscopy (STM) setup. TBG is placed on an atomically smooth dielectric consisting of monolayer WSe₂ and a thicker (approximately 30 nm thick) layer of hexagonal boron nitride (hBN)8; see Sect. 1 of Supplementary Information for fabrication details. By applying a gate voltage V_{Gate} to a graphite gate underneath, we tune the TBG charge density or, equivalently, the filling factor ν corresponding to the number of electrons per moiré unit cell. Typical TBG topography shows a moiré superlattice consisting of AA sites, where the local density of states (LDOS) originating from bands closest to the Fermi energy at charge neutrality is predominantly concentrated²⁻⁵, and intervening AB sites (Fig. 1a). Local twist angle and strain are determined by measuring distances between neighbouring AA sites^{2,3} (see Sect. 2 of the Supplementary Information). We first focus on a TBG region with local twist angle 1.32° to show experimentally that interactions play an important role even well above the magic angle of approxi-

To examine the moiré band structure, we probe Landau levels (LLs) that develop when an out-of-plane magnetic field is applied. The tunnelling conductance spectrum taken on an AB site shows two different sets of LLs observed as LDOS peaks separated by the Van Hove singularities (VHSs) (Fig. 1c,d). The LLs from the inner set, with energies bounded within the two VHSs^{7,8}, originate from band pockets around the κ and κ' high-symmetry points of the moiré Brillouin zone; we therefore denote them as κLLs (Fig. 1e). Similarly, we define the LLs outside the VHSs as γLLs since they originate from portions of the bands around the γ point. This assignment is justified by the magnetic field dependence of the observed LL spectrum (see also Supplementary Fig. S1). In particular, upon increasing the magnetic field, the zeroth γLLs (γLL_0 in the valence and conduction bands) approach the VHSs, as expected from the conduction and valence band dispersion at the γ point; the KLL energies, in contrast, do not change—consistent with the zeroth LLs expected from the Dirac-like dispersion at the κ , κ' points. Moreover, even though both κLLs and γLLs are visible on the AB sites, only the κLLs are resolved on AA sites (Supplementary Fig. S2a,b). This observation suggests that the spectral weight of

¹T. J. Watson Laboratory of Applied Physics, California Institute of Technology, Pasadena, CA, USA. ²Institute for Quantum Information and Matter, California Institute of Technology, Pasadena, CA, USA. ³Department of Physics, California Institute of Technology, Pasadena, CA, USA. ⁴Walter Burke Institute for Theoretical Physics, California Institute of Technology, Pasadena, CA, USA. ⁵Department of Physics and Astronomy, California State University, Northridge, CA, USA. ⁶National Institute for Materials Science, Tsukuba, Japan. ⁷These authors contributed equally to this work: Youngjoon Choi, Hyunjin Kim. [™]e-mail: s.nadj-perge@caltech.edu

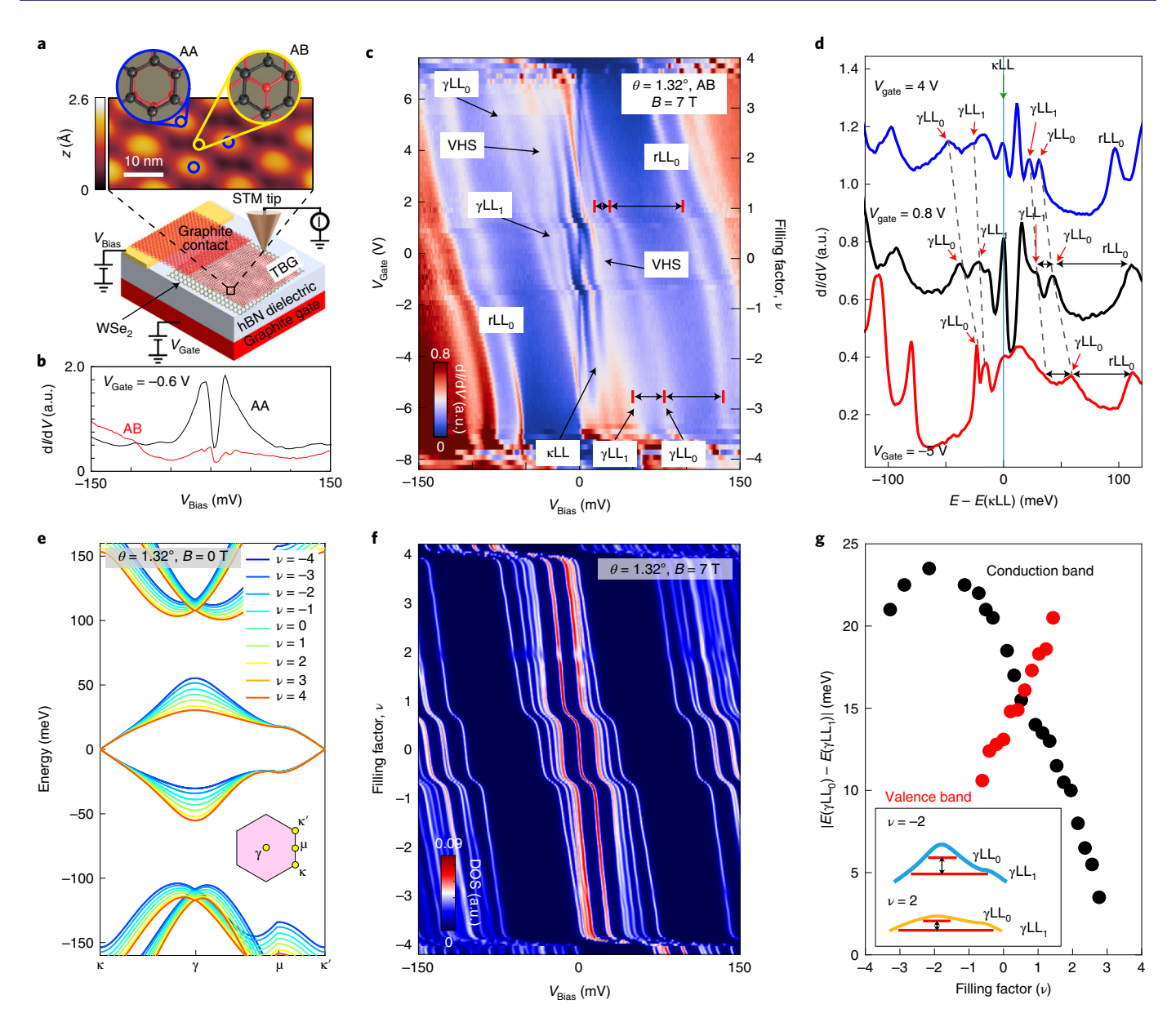


Fig. 1 | **Filling-dependent band structure deformation of TBG at twist angle** θ = 1.32°. **a**, Device schematics and TBG surface topography. TBG is placed on a monolayer WSe₂, thin hBN layer and graphite back gate. A bias voltage V_{Bias} is applied through a graphite contact placed on top. Blue and yellow circles respectively indicate AA- and AB/BA-stacked regions in the TBG moiré pattern (tunnelling set-point parameters: V_{Bias} = 100 mV, I = 20 pA). **b**, Point spectroscopy at B = 0 T near the CNP taken at an AA and an AB site; AA sites show large LDOS peaks due to VHSs. **c**, Tunnelling conductance (dI/dV) spectroscopy on an AB site versus V_{Gate} at B = 7 T (T = 2 K) showing the evolution of LLs with electrostatic doping. The LLs originating from γ and κ pockets (γ LLs and κ LLs) of the flat bands and LLs from remote bands (rLLs) are identified. The energy separation between different LLs (marked by black lines) changes with V_{Gate} (see Sect. 2 of Supplementary Information for conversion between V_{Gate} and ν). **d**, Line cuts from **c** at V_{Gate} = 4, 1 and -5 V. **e**, Calculated TBG band structure with Hartree corrections for θ = 1.32° and B = 0 T. Electron doping flattens the conduction band, while hole doping flattens the valence band. **f**, Calculated density of states with Hartree corrections as a function of filling for B = 7 T (Sects. 8 and 9 of Supplementary Information). Steps in **f** and **c** arise due to the LL spectrum gaps. **g**, γ LL₀ and γ LL₁ separation as a function of ν , showing conduction (valence) band flattening for electron (hole) doping.

the κ,κ' pockets is spatially located predominantly on AA sites while the weight of the γ pocket is distributed instead over AB sites and intermediate domain walls, in line with previous theoretical calculations 19,25,26.

Importantly, the energy separation between γLL_0 and γLL_1 changes with carrier density (Fig. 1c,d), signalling significant deformation of the moiré bands with doping even at the large twist angle 1.32°. For the conduction band, the separation is maximized at $\nu = -4$, where $E(\gamma LL_0) - E(\gamma LL_1) \approx 25$ meV, and decreases monotonically below 5 meV near $\nu = +4$ (Fig. 1g). For the valence band, the trend is reversed:

the separation between γLLs increases with filling factor (see Supplementary Fig. S3a,b, on remote bands and extracted effective mass). Further, the observed band deformations are related to neither the WSe₂ substrate used in our samples (Sect. 3 and Supplementary Fig. S4 of Supplementary Information) nor the presence of finite heterostrain (Sect. 4 of Supplementary Information). Note that a displacement field, probably present due to the single-back-gate geometry of our device, might also slightly modify the band structure with doping. However, the displacement field would change the conduction and valence bands symmetrically, in contrast to the observed

NATURE PHYSICS LETTERS

asymmetric evolution of γ LLs (Supplementary Fig. S3c,d and Sects. 6–9 of Supplementary Information).

The doping-dependent shifts between YLLs are well captured by a model that includes interaction effects deriving from the inhomogeneous charge distribution in a moiré unit cell 19-21,23,27. Starting from charge neutrality, electrons are first added or removed from states near κ , κ' that localize primarily on AA sites, creating an associated inhomogeneous electrostatic Hartree potential peaked in the AA regions. States near the γ point feel this potential less strongly compared with states near the κ point because they are relatively delocalized within the unit cell. The electrostatic potential experienced differently in each part of the moiré bands renormalizes the band dispersion. This band deformation changes upon doping because the Hartree potential depends on the filling of the moiré bands. Figure 1e presents the calculated band structures for different integer fillings at B=0 T (Sect. 6 of Supplementary Information). The conduction and valence bands deform asymmetrically with doping: the conduction (valence) band becomes flatter and the valence (conduction) band more dispersive as the filling factor increases (decreases). Consequently, in finite magnetic fields, the energy separation between yLLs also changes asymmetrically (Fig. 1g, inset). The LL spectrum evaluated with only the electrostatic Hartree potential (Fig. 1f and Sect. 9 of Supplementary Information) indeed reproduces the main features of the experimental data for this twist angle.

An interaction-induced deformation of the moiré bands completely flattens the y pocket when the twist angle approaches the magic angle value, as can be deduced from the measured evolution of yLLs (Fig. 2). To explore the twist angle dependence, we focus on an area where the angle changes over an area of approximately 600 nm and the strain is relatively low (<0.3%) (Fig. 2a). Spatially resolved measurements in this area reveal the twist-angle-dependent evolution of LLs with electrostatic doping (Fig. 2b-e). At V_{Gate} near the charge neutrality point (CNP) (Fig. 2b), we observe that, for both the valence and conduction moiré bands, the γLL₀ eventually merges with the corresponding VHS, signalling maximal band flattening. The onset of merging occurs at somewhat larger angles for the valence band (approximately 1.15°) compared with the conduction band (approximately 1.1°). Moreover, doping strongly shifts this onset. For example, in the valence band (Fig. 2c-e), the maximal band flattening moves considerably towards larger (smaller) twist angles for hole (electron) doping (see Supplementary Fig. S5 for the conduction band).

More detailed examples of the evolution of LLs, along with the development of correlated gaps in finite fields, is seen in the doping versus bias maps of Fig. 2f-h (see also Supplementary Fig. S6 for more data). At 1.23° (Fig. 2f), the γLL₀ energies are well resolved in both the valence and conduction bands between $\nu \approx -2.2$ and $\nu \approx +3.3$, beyond which one of the two merges with the corresponding VHS; in this case, the joining further occurs at the doping where the VHS lies at the Fermi energy $V_{\text{Bias}} = 0 \text{ mV}$ (see the discussion of Fig. 3). The difference in the filling factor magnitude where the conduction- and valence-band γLLs merge reflects an appreciable electron-hole asymmetry. At this large twist angle, aside from quantum Hall ferromagnetism in the zeroth kLL (responsible for the structure between $\nu = -1$ and +1), no pronounced correlated gaps are observed at the Fermi energy. As the twist angle is decreased to 1.17°, the γLL₀ in the valence band merges with the VHS at a lower $|\nu|$, and an additional correlated gap appears when the merged γLL₀ crosses the Fermi energy (Fig. 2g, black arrow). For an even lower angle of 1.15°, correlated gaps also begin to emerge on the electron-doped side after the γLL₀ merges with conductance-band VHS (Fig. 2h, black arrows). These correlated gaps correspond to Chern insulators (with Chern number *C*) that emanate from integer filling factors when electron-electron interactions are strong compared to the width of the Chern bands in finite magnetic fields^{8,28}.

Our observations suggest that such correlated phases emerge only once portions of the bands around γ become maximally flat and join with the VHS. Note also that it is expected that band deformations observed here through evolution of LLs persist down to zero magnetic field (see Sect. 5 of Supplementary Information for more detailed discussions).

To explore the development of zero-field correlated phases as a function of twist angle, we perform angle-dependent gate spectroscopy to trace out the evolution of the LDOS at the Fermi level⁸ ($V_{\text{Bias}} \approx 0$) as a function of charge density (V_{Gate}) (Fig. 3a,b). Pronounced LDOS suppression near the Fermi energy occurs at certain integer filling factors ν . For all angles, prominent suppression is observed at $\nu = \pm 4,0$, reflecting the small LDOS around the CNP ($\nu = 0$) and band gaps at full fillings ($\nu = \pm 4$). At $\nu = \pm 2, +3$, +1, we additionally observe sharp LDOS drops that can be attributed to emerging correlated gaps similar to those resolved in transport^{1,29-31}. Importantly, the observed LDOS suppressions at integer fillings begin to emerge within the same range of angles that displays considerable band flattening in finite fields (Figs. 2 and 3a and Supplementary Figs. S7 and S8). The angle onsets of the insulating regions for the conduction and valence bands (marked by dashed lines and arrows) have an electron-hole asymmetry that is also consistent with the band flattening. Spectra at $\nu = \pm 2$ taken at various twist angles (Fig. 3c,d) indeed show that LDOS suppressions originate from the development of a gap at the Fermi energy and that the $\nu = -2$ gap emerges at slightly higher angles—a further demonstration of electron-hole asymmetry. The maximal size of this half-filling gap is approximately 1.5 meV, lower than the initial reports from spectroscopic measurements²⁻⁴ but slightly larger than the activation gap extracted from transport^{1,29-31}. Note that the LDOS suppression from the observed gaps in Fig. 3c,d may also be, in part, related to the Fermi surface reconstruction due to flavour symmetry-breaking cascade^{32,33} (see also the discussion of Fig. 4). Taken together, our observations suggest a close relation between band flattening, correlated gaps and cascade physics.

A theoretical analysis of the continuum-model band structure 10,34 with interactions treated at a mean-field level in part accounts for the observed band flattening and related symmetry-breaking cascade instabilities near the magic angle (see Sect. 11 of Supplementary Information). While the doping dependence of the moiré band deformation at larger angles is well modelled by assuming only a Hartree correction (Fig. 1), near the magic angle a Hartree-only theory becomes insufficient: such theory cannot describe cascade, and, moreover, by construction, it is equivalent to the non-interacting model at charge neutrality, thus predicting unrealistically small flat-band bandwidths. Fock terms, although difficult to include in a way that produces complete quantitative matching with experiments^{21,22,35,36}, alleviate some of these qualitative shortcomings. Focusing only on the y pocket near the magic angle, Fock terms counteract Hartree-driven inversions and may thereby further stabilize band flattening (see Fig. 3e-g, and Sects. 6 and 7 of Supplementary Information for further discussion). Regardless of the exact details, the band flattening significantly amplifies the DOS at the Fermi level $(E_{\rm F})$ relative to expectations from non-interacting models (by up to a factor of approximately 4 for $\nu = 2$ and 15 for $\nu = 3$ in our model) (Fig. 3h). This interaction-driven magnification of the already-substantial DOS around the VHS accordingly promotes the symmetry-breaking cascade of electronic transitions^{32,33}. For a more quantitative treatment of the cascade instabilities, we compare the energies of unpolarized and flavour-polarized states at integer fillings for different twist angles. Depending on the model, a non-self-consistent treatment that neglects band renormalization predicts either spontaneous flavour polarization within a narrow window around the magic angle or no cascade at all (Supplementary Fig. S16). A self-consistent treatment that incorporates band flattening (Fig. 3i), by contrast, exhibits cascade behaviour over broader

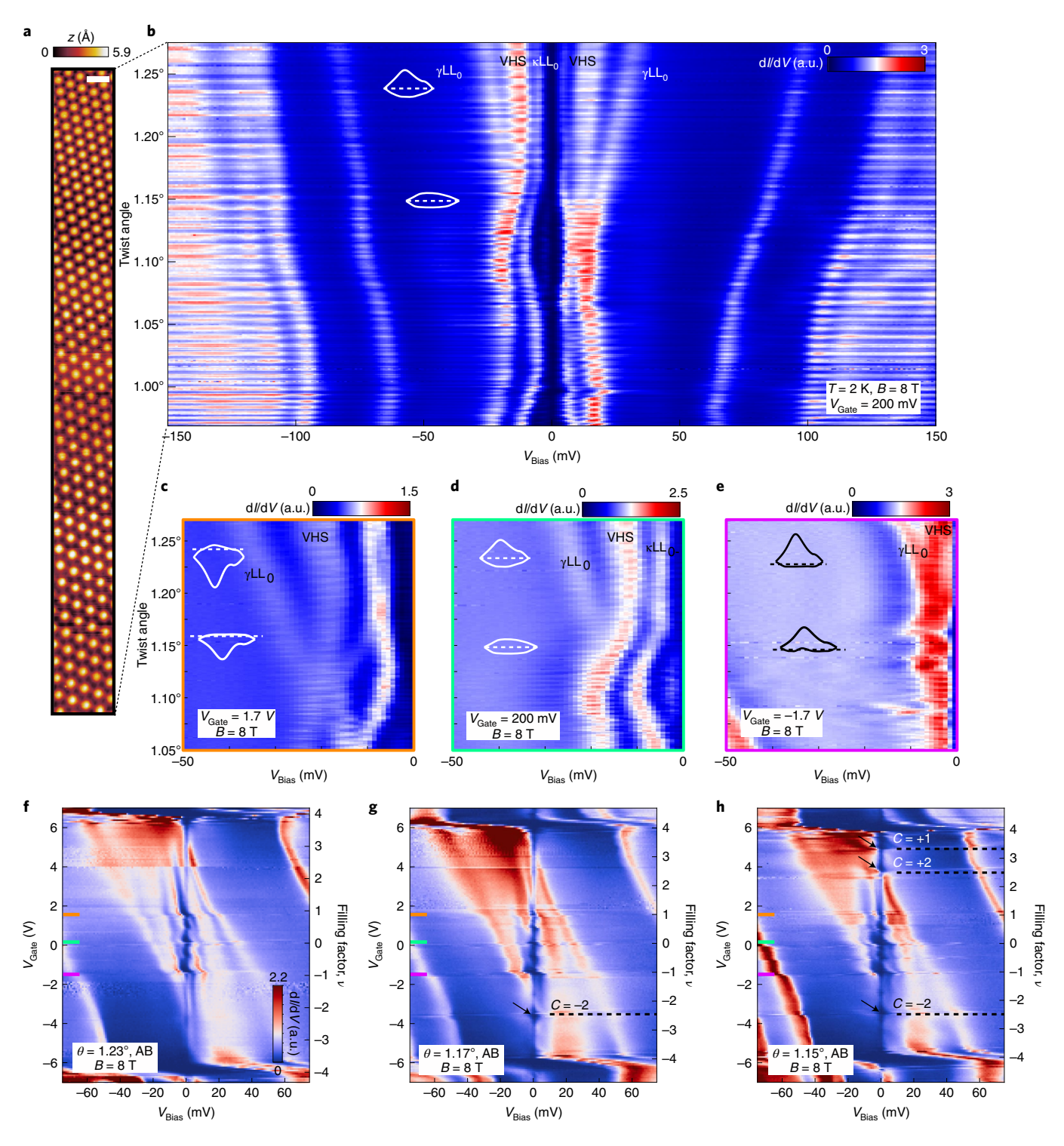


Fig. 2 | **Evolution of LLs with twist angle and correlated gaps at** B=8 **T. a**, A 590 nm ×50 nm area where the twist angle slowly changes from 1.27° to 0.97° (scale bar corresponds to 20 nm; set-point parameters are $V_{\text{Bias}}=100$ mV, I=20 pA). **b**, Spectroscopic map near the CNP ($V_{\text{Gate}}=0.2$ V) taken over the same area, averaged along the horizontal axis while the vertical axis is converted into the local twist angle. Evolution of LLs from the flat ($|V_{\text{Bias}}| < 50$ mV) and remote bands ($|V_{\text{Bias}}| > 50$ mV) is clearly resolved. **c-e**, The same plot as **b** but focusing on the evolution of the valence-band γLL₀ for $V_{\text{Gate}}=1.7$ V (**c**, electron doping), $V_{\text{Gate}}=0.2$ V (**d**, near the CNP) and $V_{\text{Gate}}=-1.7$ V (**e**, hole doping). Merging between γLL₀ and the VHS occurs at higher twist angle as V_{Gate} is reduced. The insets in **b-e** sketch the band structure and Fermi level near $\theta=1.23^{\circ}$ and $\theta=1.15^{\circ}$. A smooth signal background is subtracted to enhance LL visibility. **f-h**, Point spectroscopy for $\theta=1.23^{\circ}$ (**f**), 1.17° (**g**) and 1.15° (**h**). Black arrows in **g** and **h** indicate emerging correlated Chern phases^{7,8} after the γLL₀ merges with the VHS. Colour-coded lines show V_{Gate} values used in **c-e**.

twist angle windows whose widths depend strongly on filling, in agreement with experimental data on the electron-doped side of Fig. 3a (see also Supplementary Fig. S13). These findings are also

in agreement with recent theoretical calculations²⁴ that predict a broader twist angle window where correlated physics is observed when band flattening is taken into account.

NATURE PHYSICS LETTERS

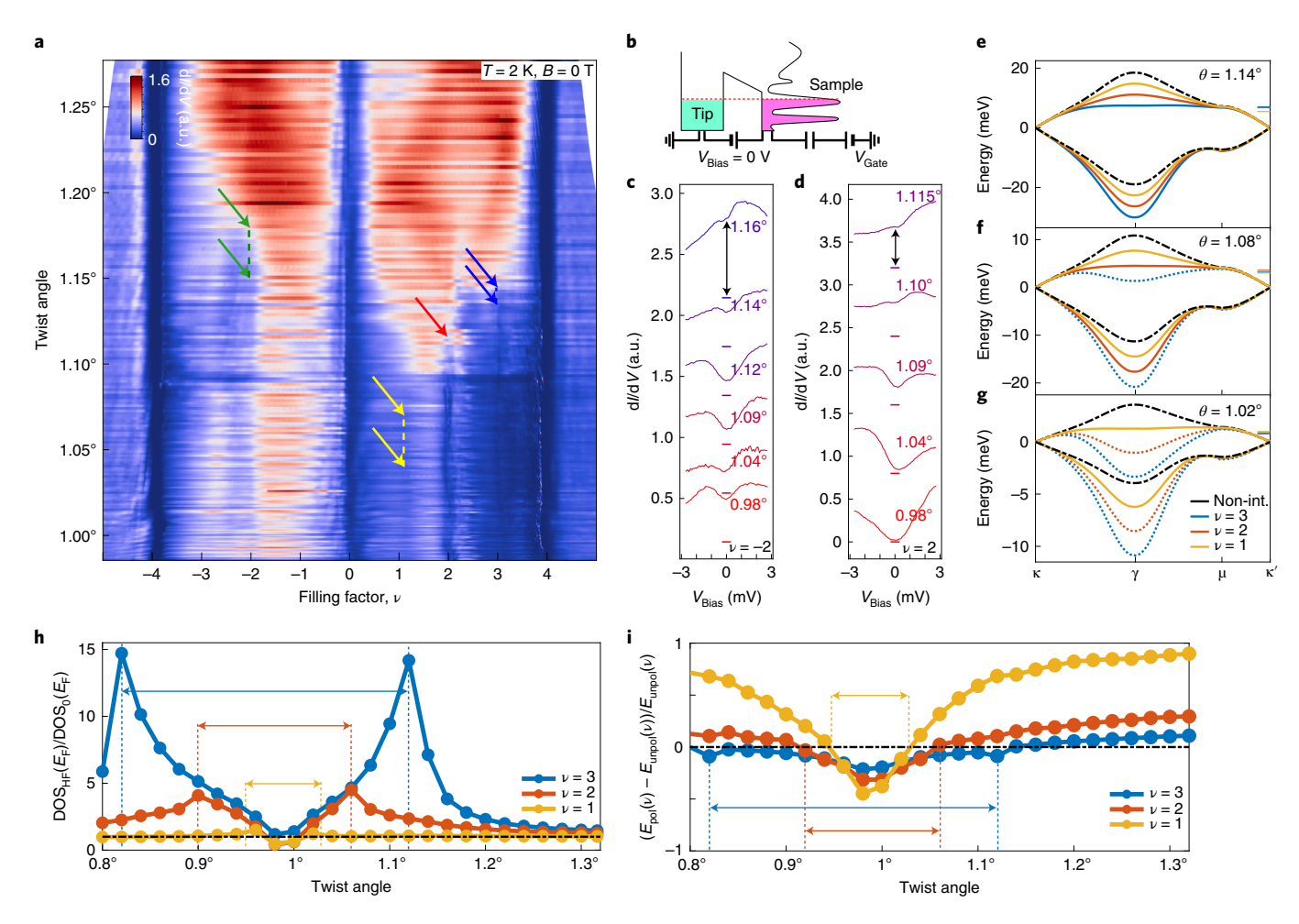


Fig. 3 | Emergence of zero-field correlated gaps and symmetry-breaking cascade. **a**, Angle and filling factor dependence of d/dV near E_F ($V_{Bias} = 0.3$ mV) for B = 0 T taken on the same area as in Fig. 2a,b. Correlated gaps at $\nu = -2$, +1, +2, +3, observed as an abrupt drop in d/dV (that is, LDOS), develop only below certain twist angles, in contrast to regions between the flat and remote bands ($\nu = \pm 4$) where the LDOS is small for any angle. Coloured arrows indicate the onset angle range of the corresponding LDOS suppression regions. **b**, Measurements in **a** are taken by fixing $V_{Bias} \approx 0$ so that the STM tip probes LDOS near the E_F while V_{Gate} is swept. **c**,**d**, Spectroscopy for $\nu = -2$ (**c**) and $\nu = +2$ (**d**) at different local twist angles (offset for clarity), taken on AB sites in the same area. Line colour coding corresponding to bars in **a** indicates twist angle. Correlated gaps are observed only below a certain onset angle consistent with **a** (wiggles above this angle are of different origin; Supplementary Fig. S10). **e**-**g**, Interaction-renormalized band structures at different integer fillings, calculated assuming unpolarized ground states (see main text and Sect. 11 of Supplementary Information). Horizontal lines indicate the relevant chemical potentials. In cases where polarized states are favourable, dotted lines are used. The non-interacting band structure is shown in black. **h**, Twist angle dependence of the DOS at E_F obtained from the interaction-corrected unpolarized band structure, normalized by the non-interacting DOS. Peaks signal maximal band flattening as seen in **e**-**g**. **i**, Energy change for polarized (cascaded) states relative to unpolarized states. Interaction-driven band flattening significantly extends the range of angles, marked by arrows in **h** and **i**, where this relative energy change is negative and polarization becomes energetically favourable (Sect. 11 of Supplementary Information).

Our observations reconcile the apparent discrepancy between the predominance of interactions implied by the emergence of correlated phases around the magic angle and previous measurements, including (i) a large Dirac velocity around the CNP^{1,8,9}, (ii) a total bandwidth exceeding 40 meV (refs. 2-6,32) and (iii) a large separation of the VHSs2-5, that seem at odds with supposedly crucial aspects of the band theory predictions. These quantities (Dirac velocity, total bandwidth and the VHS separation) appear not to be essential. For example, Supplementary Fig. S11 shows that the measured Dirac velocity and VHS separation are even smaller at 1.18° than at 1.04°, while signatures of strongly correlated phases (for example, symmetry-breaking cascade and correlated gaps) appear at the latter twist angle but not the former. Instead, we identify the interaction-driven flattening of the moiré bands around the γ pockets, with the consequent increase in the density of states, as the decisive feature needed for the formation of correlated phases.

Our conclusions here are also in line with theoretical works that consider band flattening in TBG due to Hartree corrections^{19–24}. We again emphasize, however, that Hartree-only corrections do not capture TBG physics near the CNP (see Sect. 7 of Supplementary Information and refs. ^{21,35}).

In addition to correlated gaps pinned to integer fillings $\nu=\pm 2,+1,+3$, we also observe several other interaction-driven features near the magic angle that have not been discussed in previous STM measurements (Fig. 4). For example, prominent LDOS suppressions at the Fermi level are visible in both the $2<\nu<3$ and $-3<\nu<-2$ doping regions (Fig. 4b–d). Of these two regions, the feature between $\nu=+2$ and +3 has a 'tilted V' shape at small bias voltages, which can be largely understood as a consequence of the relative prominence of the flavour polarization in the conduction band compared with the valence band⁸ (see also Fig. 3a–d). There, two of the four flavours are pushed away from the Fermi

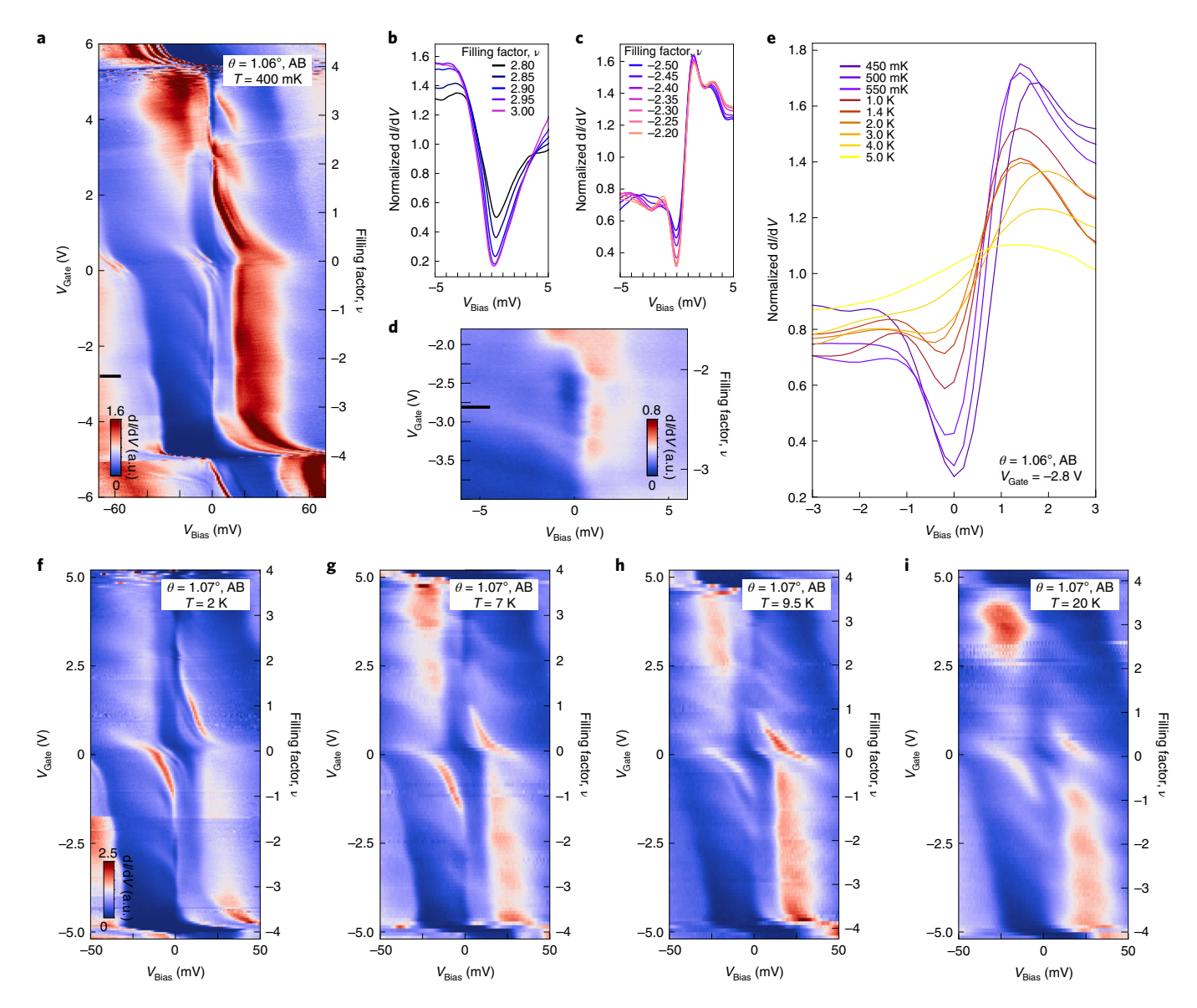


Fig. 4 | Temperature dependence of correlated gaps around $\nu=\pm2$ **and the symmetry-breaking cascade. a**, Point spectra as a function of V_{Gate} for $\theta=1.06^{\circ}$ at B=0 T. **b,c**, dI/dV spectra for filling factors ranging from $\nu=2.8$ to $\nu=3.0$ (**b**) and from $\nu=-2.5$ to $\nu=-2.2$ (**c**). **d**, High-resolution point spectra of **a** focusing on the soft gap between $\nu=-2$ and -3. **e**, dI/dV spectra at $V_{\text{Gate}}=-2.8$ V (as indicated by black lines in **a,d**) for temperatures ranging from 450 mK to 5 K at the same tip location as **a. f-i**, Point spectra as a function of V_{Gate} for $\theta=1.07^{\circ}$ at temperatures T=2 K (**f**), T=7 K (**g**), T=9.5 K (**h**) and T=20 K (**i**). As temperature increases, the cascade features become more pronounced, and their onset more closely follows integer filling factors, hinting at a characteristic cascade temperature scale of $T\approx20$ K, as noted previously³².

energy by strong interactions³², consistent with the LDOS's being predominantly shifted to higher energy (Fig. 4a,b) and resulting in an asymmetric spectrum down to the Fermi energy, as seen in compressibility measurements³². In contrast, the spectrum between $\nu = -2$ and -3 exhibits a slightly different shape that cannot be fully explained by a simple flavour-symmetry-breaking cascade that produces a large overall asymmetry. Additionally, this doping range also shows a clear, more symmetric gapped feature at small bias voltages (Fig. 4e). The corresponding gap, spanning almost the entire filling range $-3 < \nu < -2$ (Fig. 4d), reaches its maximal size of $2\Delta \approx 1.1$ meV. Also, it becomes prominent only below $\theta = 1.16^{\circ}$ (Supplementary Fig. S7) and gradually recedes with temperature and disappears above 5-7 K (Fig. 4e). The gap size as well the temperature dependence of this feature are similar to the gap at $\nu = -2$; however, the filling range observed here is unusually large and cannot be explained simply by non-interacting effects (Supplementary

Fig. S10). Furthermore, the gap extends over a filling range comparable to that at which superconductivity has been observed in transport at similar angles for TBG on WSe2 (ref. 31) as well as in many hBN-only encapsulated devices^{29,30,37}. This correspondence indicates that the observed feature may be related to superconductivity itself or signals the possible existence of a pseudo-gap phase that precedes superconductivity³⁸. Regardless of its exact origin, the pronounced suppression (instead of increase) of the LDOS near the Fermi energy, together with symmetry-breaking cascade features, for fillings where superconductivity is anticipated may suggest either an electronic pairing origin³⁹ or a regime of strong-coupling superconductivity, as recently pointed out for magic-angle trilayer graphene^{40,41}. Another interesting observation is that, while the gap-like features at the Fermi energy become weaker with increasing temperature, features at higher energies (previously identified to be related to symmetry-breaking cascade NATURE PHYSICS LETTERS

transitions^{7,8,33}) are enhanced; see the temperature evolution in Fig. 4f–i. The relation of these features and various recently reported phases that emerge at elevated temperatures^{42,43} remains a subject for future investigations.

Online content

Any methods, additional references, Nature Research reporting summaries, source data, extended data, supplementary information, acknowledgements, peer review information; details of author contributions and competing interests; and statements of data and code availability are available at https://doi.org/10.1038/s41567-021-01359-0.

Received: 3 February 2021; Accepted: 16 August 2021; Published online: 4 November 2021

References

- Cao, Y. et al. Correlated insulator behaviour at half-filling in magic-angle graphene superlattices. *Nature* 556, 80–84 (2018).
- Kerelsky, A. et al. Maximized electron interactions at the magic angle in twisted bilayer graphene. *Nature* 572, 95–100 (2019).
- Choi, Y. et al. Electronic correlations in twisted bilayer graphene near the magic angle. *Nat. Phys.* 15, 1174–1180 (2019).
- Xie, Y. et al. Spectroscopic signatures of many-body correlations in magic-angle twisted bilayer graphene. Nature 572, 101–105 (2019).
- Jiang, Y. et al. Charge order and broken rotational symmetry in magic-angle twisted bilayer graphene. *Nature* 573, 91–95 (2019).
- Tomarken, S. L. et al. Electronic compressibility of magic-angle graphene superlattices. *Phys. Rev. Lett.* 123, 046601 (2019).
- Nuckolls, K. P. et al. Strongly correlated Chern insulators in magic-angle twisted bilayer graphene. *Nature* 588, 610–615 (2020).
- 8. Choi, Y. et al. Correlation-driven topological phases in magic-angle twisted bilayer graphene. *Nature* **589**, 536–541 (2021).
- Park, J. M., Cao, Y., Watanabe, K., Taniguchi, T. & Jarillo-Herrero, P. Flavour Hund's coupling, Chern gaps and charge diffusivity in moiré graphene. Nature 592, 43–48 (2021).
- Bistritzer, R. & MacDonald, A. H. Moiré bands in twisted double-layer graphene. Proc. Natl Acad. Sci. USA 108, 12233–12237 (2011).
- Lopes dos Santos, J. M. B., Peres, N. M. R. & Castro Neto, A. H. Graphene bilayer with a twist: electronic structure. *Phys. Rev. Lett.* 99, 256802 (2007).
- Uchida, K., Furuya, S., Iwata, J.-I. & Oshiyama, A. Atomic corrugation and electron localization due to moiré patterns in twisted bilayer graphenes. *Phys. Rev. B* 90, 155451 (2014).
- Jung, J., Raoux, A., Qiao, Z. & MacDonald, A. H. Ab initio theory of moiré superlattice bands in layered two-dimensional materials. *Phys. Rev. B* 89, 205414 (2014).
- Nam, N. N. T. & Koshino, M. Lattice relaxation and energy band modulation in twisted bilayer graphene. *Phys. Rev. B* 96, 075311 (2017).
- Carr, S., Fang, S., Zhu, Z. & Kaxiras, E. Exact continuum model for low-energy electronic states of twisted bilayer graphene. *Phys. Rev. Res.* 1, 013001 (2019).
- Guinea, F. & Walet, N. R. Continuum models for twisted bilayer graphene: effect of lattice deformation and hopping parameters. *Phys. Rev. B* 99, 205134 (2019).
- Bi, Z., Yuan, N. F. Q. & Fu, L. Designing flat bands by strain. *Phys. Rev. B* 100, 035448 (2019).
- Parker, D. E., Soejima, T., Hauschild, J., Zaletel, M. P. & Bultinck, N. Strain-induced quantum phase transitions in magic-angle graphene. *Phys. Rev. Lett.* 127, 027601 (2021).

 Guinea, F. & Walet, N. R. Electrostatic effects, band distortions, and superconductivity in twisted graphene bilayers. *Proc. Natl Acad. Sci. USA* 115, 13174–13179 (2018).

- Goodwin, Z. A. H., Vitale, V., Liang, X., Mostofi, A. A. & Lischner, J. Hartree theory calculations of quasiparticle properties in twisted bilayer graphene. *Electron. Struct.* 2, 034001 (2020).
- Cea, T., Walet, N. R. & Guinea, F. Electronic band structure and pinning of Fermi energy to Van Hove singularities in twisted bilayer graphene: a self-consistent approach. *Phys. Rev. B* 100, 205113 (2019).
- Cea, T. & Guinea, F. Band structure and insulating states driven by Coulomb interaction in twisted bilayer graphene. *Phys. Rev. B* 102, 045107 (2020).
- Rademaker, L., Abanin, D. A. & Mellado, P. Charge smoothening and band flattening due to Hartree corrections in twisted bilayer graphene. *Phys. Rev. B* 100, 205114 (2019).
- Klebl, L., Goodwin, Z. A. H., Mostofi, A. A., Kennes, D. M. & Lischner, J. Importance of long-ranged electron–electron interactions for the magnetic phase diagram of twisted bilayer graphene. *Phys. Rev. B* 103, 195127 (2021).
- Rademaker, L. & Mellado, P. Charge-transfer insulation in twisted bilayer graphene. *Phys. Rev. B* 98, 235158 (2018).
- Carr, S., Fang, S., Po, H. C., Vishwanath, A. & Kaxiras, E. Derivation of Wannier orbitals and minimal-basis tight-binding Hamiltonians for twisted bilayer graphene: first-principles approach. *Phys. Rev. Res.* 1, 033072 (2019).
- Calderón, M. J. & Bascones, E. Interactions in the 8-orbital model for twisted bilayer graphene. *Phys. Rev. B* 102, 155149 (2020).
- Saito, Y. et al. Hofstadter subband ferromagnetism and symmetry-broken Chern insulators in twisted bilayer graphene. Nat. Phys. 17, 478–481 (2021).
- Yankowitz, M. et al. Tuning superconductivity in twisted bilayer graphene. Science 363, 1059–1064 (2019).
- 30. Lu, X. et al. Superconductors, orbital magnets and correlated states in magic-angle bilayer graphene. *Nature* **574**, 653–657 (2019).
- Arora, H. S. et al. Superconductivity in metallic twisted bilayer graphene stabilized by WSe₂. Nature 583, 379–384 (2020).
- Zondiner, U. et al. Cascade of phase transitions and Dirac revivals in magic-angle graphene. *Nature* 582, 203–208 (2020).
- 33. Wong, D. et al. Cascade of electronic transitions in magic-angle twisted bilayer graphene. *Nature* **582**, 198–202 (2020).
- Koshino, M. et al. Maximally localized wannier orbitals and the extended Hubbard model for twisted bilayer graphene. Phys. Rev. X 8, 031087 (2018).
- Xie, M. & MacDonald, A. H. Nature of the correlated insulator states in twisted bilayer graphene. *Phys. Rev. Lett.* 124, 097601 (2020).
- Xie, M. & MacDonald, A. H. Weak-field Hall resistivity and spin/valley flavor symmetry breaking in MAtBG. Preprint at https://arxiv.org/abs/2010.07928 (2020).
- 37. Cao, Y. et al. Unconventional superconductivity in magic-angle graphene superlattices. *Nature* **556**, 43–50 (2018).
- Hofmann, J. S., Berg, E. & Chowdhury, D. Superconductivity, pseudogap, and phase separation in topological flat bands. *Phys. Rev. B* 102, 201112 (2020).
- Bernevig, B. A. et al. Twisted bilayer graphene. V. Exact analytic many-body excitations in Coulomb Hamiltonians: charge gap, Goldstone modes, and absence of Cooper pairing. *Phys. Rev. B* 103, 205415 (2021).
- Park, J. M., Cao, Y., Watanabe, K., Taniguchi, T. & Jarillo-Herrero, P. Tunable strongly coupled superconductivity in magic-angle twisted trilayer graphene. *Nature* 590, 249–255 (2021).
- Hao, Z. et al. Electric field tunable unconventional superconductivity in alternating twist magic-angle trilayer graphene. Science 371, 1133–1138 (2021).
- Saito, Y. et al. Isospin Pomeranchuk effect in twisted bilayer graphene. Nature 592, 220–224 (2021).
- 43. Rozen, A. et al. Entropic evidence for a Pomeranchuk effect in magic-angle graphene. *Nature* **592**, 214–219 (2021).

Publisher's note Springer Nature remains neutral with regard to jurisdictional claims in published maps and institutional affiliations.

© The Author(s), under exclusive licence to Springer Nature Limited 2021

Data availability

The data reported in Figs. 1–4 can be found on zenodo: https://zenodo.org/record/5173159. Other data that support the findings of this study are available from the corresponding authors on reasonable request.

Code availability

The code that supports the findings of this study is available from the corresponding authors on reasonable request.

Acknowledgements

The authors acknowledge discussions with F. Guinea, F. von Oppen, and G. Refael. Funding: This work has been primarily supported by NSF grants DMR-2005129 and DMR-172336; and Army Research Office under Grant Award W911NF17-1-0323. Part of the STM characterization has been supported by NSF CAREER programme (DMR-1753306). Nanofabrication efforts have been in part supported by DOE-QIS programme (DE-SC0019166). S.N.-P. acknowledges support from the Sloan Foundation. J.A. and S.N.-P. also acknowledge support of the Institute for Quantum Information and Matter, an NSF Physics Frontiers Center with support of the Gordon and Betty Moore Foundation through Grant GBMF1250; C.L. acknowledges support from the Gordon and Betty Moore Foundations EPiQS Initiative (grant GBMF8682). A.T. and J.A. are grateful for the support of the Walter Burke Institute for Theoretical Physics at Caltech.

Y.P. acknowledges support from the startup fund from California State University, Northridge. Y.C. and H.K. acknowledge support from the Kwanjeong Fellowship.

Author contributions

Y.C. and H.K. fabricated samples with the help of R.P. and Y.Z., and performed STM measurements. Y.C., H.K. and S.N.-P. analysed the data. C.L. and Y.P. implemented TBG models. C.L., Y.P. and A.T. provided theoretical analysis of the model results supervised by J.A. S.N.-P. supervised the project. Y.C., H.K., C.L., Y.P., A.T., J.A. and S.N.-P. wrote the manuscript with input from other authors.

Competing interests

The authors declare no competing interests.

Additional information

Supplementary information The online version contains supplementary material available at https://doi.org/10.1038/s41567-021-01359-0.

Correspondence and requests for materials should be addressed to Stevan Nadj-Perge.

Peer review information *Nature Physics* thanks the anonymous reviewers for their contribution to the peer review of this work.

Reprints and permissions information is available at www.nature.com/reprints.